

Magnetic phases of electron-doped, infinite-layer $\text{Sr}_{1-x}\text{La}_x\text{CuO}_2$ from first-principles density functional calculations.

Alpin N. Tatan^{1,2}, Jun Haruyama², and Osamu Sugino^{1,2}

¹ Department of Physics, Graduate School of Science, The University of Tokyo, 7-3-1 Hongo, Bunkyo-ku, Tokyo, 113-0033, Japan.

² The Institute for Solid State Physics, The University of Tokyo, Kashiwanoha 5-1-5, Kashiwa, Chiba, 277-8581, Japan.

1 Abstract

The magnetic phases of electron-doped, infinite-layer $\text{Sr}_{1-x}\text{La}_x\text{CuO}_2$ are elucidated by first-principles density functional calculations. We describe the antiferromagnetic parent state, metallic phase transition, lattice structure and magnetic anisotropy evolution upon doping, as well as pressure-induced changes to the density of states at Fermi level that are consistent with experiments where comparison is possible. We investigate low-energy states with multiple magnetic configurations and study their specific heat coefficients and magnetic exchange coupling, as well as the density of states at Fermi level. The latter quantity is used to study the effects of spin fluctuations on the electronic structure of this strongly correlated material.

2 Introduction

Superconductivity can be achieved by doping cuprates with holes or electrons from the antiferromagnetic (AFM) phase [1]. This phase persists to much higher doping and coexists with superconductivity in electron-doped cuprates [2, 3, 4, 5, 6, 7]. Experiments on these materials have been mostly performed on $\text{RE}_{2-x}\text{Ce}_x\text{CuO}_4$ compounds. Unfortunately, the magnetic rare-earth (RE) atoms can mask the necessary information from the CuO_2 plane [7]. Another electron-doped cuprate is the $\text{Sr}_{1-x}\text{La}_x\text{CuO}_2$ infinite layer (SLCO, see Figure 1). However, the synthesis of SLCO single crystal has not been possible: only polycrystalline [8] or thin films [9] have been prepared. Information on spin arrangements from ideal techniques (i.e., neutron scattering) is not yet available, and other probes such as nuclear magnetic resonance (NMR) have limitations [10, 11, 12]. For example, Ref. [10] could deduce the presence of AFM order based on the observed NMR wipeout effect and analysis of its linewidths, but details such as the magnitude of magnetic moments on copper sites could not be determined from their experiments.

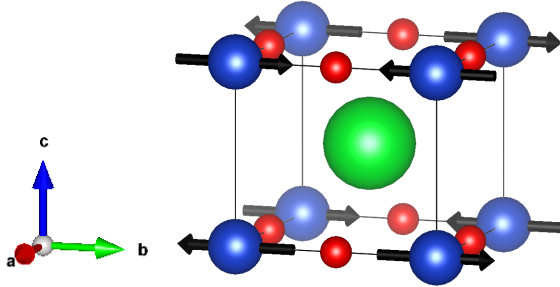


Figure 1: The unit cell of infinite-layered $\text{Sr}_{1-x}\text{La}_x\text{CuO}_2$ (black lines) with Sr/La, O, and Cu atoms represented by green, red, and blue spheres, respectively. The arrows indicate magnetic moments on copper sites, aligned along the Cu-O-Cu direction in this illustration.

Angular magnetoresistance (AMR) measurement is an interesting, albeit indirect, technique for deducing magnetic order. Angular dependence results from the correlation between spin arrangements and conduction electrons. AMR oscillations have also previously been attributed to the coexistence of antiferromagnetism and superconductivity in $\text{RE}_{2-x}\text{Ce}_x\text{CuO}_4$ compounds [13]. Ref. [7, 9] studied AMR oscillations from SLCO samples and explained them as due to AFM order in the CuO_2 planes. In particular, they found a modification of oscillation pattern due to a change in magnetic alignment as a function of doping levels. It is deduced that the Cu spins of the less doped sample are antiferromagnetically aligned along the Cu-O-Cu direction, as in the case of the undoped compound, while those of the more doped sample align along the Cu-Cu direction. The origin for this change has been suggested as spin dilution leading to a less rigid spin structure, which should be investigated further.

First-principles calculations based on density functional theory (DFT) are useful tools for complementing experimental investigations. The correlated nature of electrons in cuprates, however, has been the bane of parameter-free DFT studies in these materials. For example, the local density or generalized gradient approximations (LDA/GGA) cannot describe the AFM parent compound without invoking empirical parameters, e.g., the Hubbard U coefficient [2, 14]. This feat is recently accomplished with the strongly constrained and appropriately normed (SCAN) functional [15], which provides accurate parameter-free description of La- [16, 17], Y- [18], Bi- [19], and Hg-cuprates [20] in undoped and doped phases. Interestingly, SCAN predicts persisting antiferromagnetism in Y- and Hg-based cuprates even for doped compounds [18, 20]. Motivated by these results, here we utilize SCAN to study the evolution of antiferromagnetic phases from SLCO in the underdoped region of the metal-insulator phase boundary. First, we will confirm the antiferromagnetic insulator phase of the parent compound. Second, we will demonstrate the metallic phase transition and inspect the evolution of relaxed structural parameters in the doped compounds. Third, we will check the AMR results [7] for the AFM alignment (i.e., the easy axis) for the $x = 0.125$ doped compounds. Fourth, we will highlight some low-energy magnetic phases found near the phase boundary and briefly comment how these phases may contribute to high-temperature superconductivity in this material by examining relevant parameters such as the density of states at Fermi level, $N(0)$, magnetic exchange coupling, J , and specific heat coefficient, γ .

3 Computational methods

Generally, we follow the preceding SCAN studies for cuprates [16, 17, 18, 19, 20]. Calculations are performed with the pseudopotential projector augmented-wave (PAW) method [21] implemented in the Vienna ab initio simulation package (VASP) [22, 23] with an energy cutoff of 550 eV for the plane-wave basis set. Exchange–correlation effects are treated using the SCAN meta-GGA scheme [15]. Structures are optimized using blocked-Davidson and preconditioned conjugate gradient algorithms with an atomic force threshold of 0.01 eV/Å and a total energy threshold of 10^{-5} eV. Γ -centered k-point mesh with spacing of 0.12 \AA^{-1} is used for structure optimizations. We tighten the energy threshold to 10^{-8} eV and utilize denser k-point meshes (0.08 \AA^{-1} or less) in total energy and density of states calculations using the tetrahedron method with Blöchl corrections [24]. Most of the calculations are performed in collinear mode. For comparison with the AMR results [7, 9], non-collinear calculations that consider spin-orbit coupling effects are performed at $x = 0$ and $x = 0.125$ to compute the magnetic anisotropy energy (MAE), defined as:

$$\text{MAE}_{xyz} = E_{xyz} - E_c \quad (1)$$

where E_{xyz} and E_c are, respectively, the total energies calculated with magnetic moments on copper sites aligned along a direction shown by $[xyz]$ and along the c -axis in the coordinate system depicted in Figure 1. To match with Ref. [7, 9], we consider MAE calculations for AFM alignments along the lines connecting Cu-O-Cu atoms (i.e., $[xyz] = [100]$) and Cu-Cu atoms (i.e., $[xyz] = [110]$) in the CuO_2 plane, respectively. Electron doping is achieved by substituting trivalent La on divalent Sr sites using the supercell method.

The ‘G’ and ‘C’ magnetic orders, as well as the nonmagnetic ‘N’ configuration are set as initial parameters. The ‘G’ configuration is exemplified in Figure 1. The ‘C’ order is very similar to this, but without AFM order along the c -axis. It is thus a two-dimensional AFM structure with identical alignment across the CuO_2 planes. The nomenclature follows Ref. [25] and has also been used in recent works [18, 26]. In the underdoped SLCO region, we expect a number of local minima consisting of magnetic configurations beyond these single-phase choices to which our self-consistent optimizations can converge. In addition to finding the ground state with the robust preconditioned conjugate gradient algorithm, local minima can also be found using the blocked-Davidson scheme as long as convergence is reached. As the latter scheme is not robust for finding the ground state, we use it to conveniently find nearby local minima in standard self-consistent calculations. We utilize this method in a screening procedure as illustrated in Figure 2 where we look for interesting changes of the electronic structure in these local minima [27, 28]. The increase in the density of states at the Fermi level ($N(0)$), for example, can be taken as a sign in favor of Cooper pair formation [29]. We also estimate the magnetic exchange coupling, specific heat coefficients, and pressure effects for analysis in comparison with available experiments.

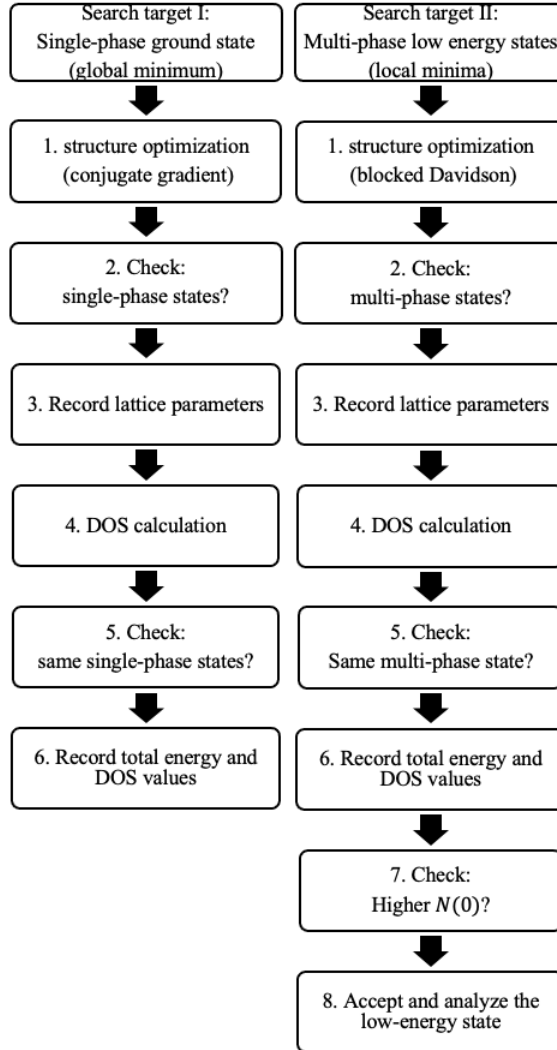


Figure 2: Calculation procedure for finding the ground and low-energy states. The conjugate gradient algorithm is robust while the blocked Davidson scheme may converge to a low-energy state instead of the ground state. The latter is utilized to screen the low-energy multiphase states that has increased DOS value at Fermi level $N(0)$.

4 Results and discussions

4.1 The AFM insulator phase of the parent compound

The optimized lattice parameters of the parent compound take the value of $a = 3.910 \text{ \AA}$, $c = 3.444 \text{ \AA}$, which are less than 1 percent away from the experimental values ($a = 3.927 \text{ \AA}$, $c = 3.435 \text{ \AA}$) in Ref. [30]. These values are insensitive to the choice of magnetic configurations. The ground state is the ‘G’ configuration, with the ‘C’ and ‘N’ configurations lying 3.28 and 59.11 meV above it. The magnetic moment at copper site is calculated by integrating the magnetic moment within a PAW sphere of radius 1.164 \AA , as set by the pseudopotential for Cu. For the parent compound, this is approximately $\pm 0.47 \mu_B$ per atom.

The valence and conduction bands near the Fermi level (Figure 3(a)) are primarily of Cu $3d$ and O $2p$ orbital characters, as expected from crystal field theory. The bandgap opens when AFM order exists. For the ground state, an indirect (direct) band gap of ≈ 0.35 (1.1) eV exists between the R and A points of the AFM first Brillouin zone. Interestingly, this gap is reduced to only approximately 0.2 eV when the structure takes the ‘C’ configuration. Since the latter only has in-plane AFM order, this suggests the importance of interplanar interactions in the overall electronic structure of this material.

4.2 Metallic phase transition in the doped compounds

A transition to a metallic phase is achieved by doping the parent structure. This is demonstrated in Figure 3(b), where 1 La has been substituted for Sr in a $\sqrt{2} \times \sqrt{2} \times 2$ supercell in a ‘G’ magnetic configuration. The band gap closes and the Fermi level moves to higher energy, indicating a metallic phase transition under the electron doping condition.

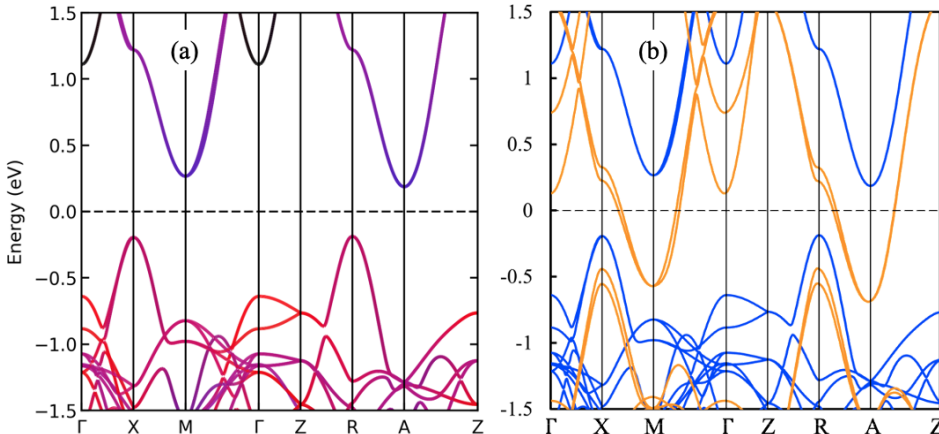


Figure 3: (a): The projected band structure of SrCuO₂ computed with $\sqrt{2} \times \sqrt{2} \times 2$ cell. The contribution from Cu d (blue) and O p (red) orbitals are shown. Together, they form most of the low-energy bands (purple) near the Fermi level E_F , which is set to zero. Only the spin-up configuration is shown. This plot is generated with the sumo code [31]. (b): The band structure for SLCO with $x = 0$ (blue) and $x = 0.25$ (orange). A metallic phase transition with electron doping character is achieved.

Subsequently, we expand the supercells to simulate lower La concentrations. The relaxed lattice parameters evolve with x as shown in Figure 4, where the doped compounds are metallic. The value of the lattice parameters and their x -dependence are in good agreement with experiment [30] as shown in Figure 4. The LDA, on the other hand, significantly underestimates the lattice parameters, which may be ascribed to the well-known problem of ‘overbinding’. This better agreement for SCAN is not simply ascribed to its better performance for magnetism, as our SCAN structures yield similar values for both magnetic and non-magnetic cells. Instead, this showcases how the LDA and SCAN functionals treat bonds between atoms differently; indeed, accurate description of interatomic bonds is one of the focus areas of SCAN in its construction [15].

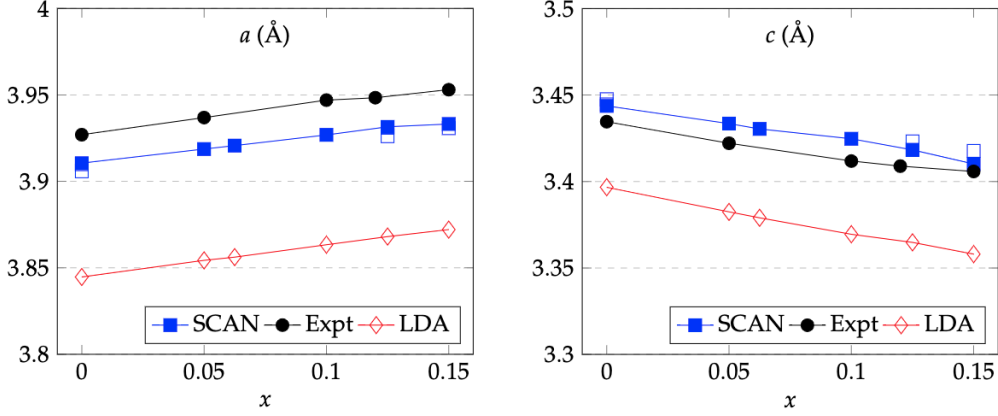


Figure 4: The lattice parameters plotted against La concentration x . The open and closed symbols denote values without and with magnetic order, respectively. Experimental values are from Ref. [30].

4.3 Magnetic anisotropy energy at $x = 0$ and $x = 0.125$

Calculations considering non-collinear magnetism and spin-orbit coupling are performed for $x = 0$ and $x = 0.125$ to compute the magnetic anisotropy energy (MAE) for comparison with the $x = 0.12$ samples measured in the AMR experiments [7, 9]. We use equation (1) for the respective alignments and summarize the results in Table 1.

Alignment	$x = 0$	$x = 0.125$
[100] (Cu-O-Cu)	-0.022	+0.017
[110] (Cu-Cu)	-0.002	+0.020

Table 1: Magnetic anisotropy energy (MAE) per Cu atom of $\text{Sr}_{1-x}\text{La}_x\text{CuO}_2$ for the magnetic moments at copper sites aligned in-plane along the [100] (Cu-O-Cu) and [110] (Cu-Cu) directions. Values are in meV and relative to the total energy for structures with magnetic moments at copper sites aligned along the [001] (c -axis) direction. The $[xyz]$ directions refer to the unit cell coordinates (Figure 1).

The MAE in cuprates is known to have small values. For example, the Li-based cuprate, Li_2CuO_2 has values between 0.045-0.078 meV per Cu atom, determined from magnetization jump and neutron scattering experiments [32, 33]. Hence, our computed MAE value ≈ 0.02 meV is quite reasonable. The results indicate a preferential in-plane spin alignment along the Cu-O-Cu direction over the other directions for $x = 0$, and along the c -axis at $x = 0.125$. The small MAE suggests that it should be fairly common to obtain samples with either alignment, subject to synthesis conditions. The apparent degeneracy of in-plane orientations (along the Cu-Cu and Cu-O-Cu directions) suggests a less rigid AFM order in the doped compounds, which agrees with the AMR reports of Ref. [7, 9].

4.4 Low-energy magnetic phases near the phase boundary

4.4.1 General trend of total energies

Config.	$x = 0$	$x = 0.0625$	$x = 0.1$	$x = 0.125$
N	+59.11	+50.54	+40.16	+37.85
C	+3.28	-0.09	-0.12	-0.19
‘Multiphase’		+31.77 (G+E)	+9.39 (G+C+N)	+22.79 (G+N)

Table 2: Total energy E per Cu atom of $\text{Sr}_{1-x}\text{La}_x\text{CuO}_2$ relative to the magnetic ‘G’-state in units of meV. The values for each x are computed on $\sqrt{2} \times \sqrt{2} \times 2$, $4 \times 4 \times 2$, $\sqrt{2} \times \sqrt{2} \times 10$, and $\sqrt{2} \times \sqrt{2} \times 4$ supercells, respectively. The nomenclature (G, C, E) follows Ref. [25]. Only multiphase states with increased $N(0)$ are shown.

The total energies of relaxed structures relative to the magnetic ‘G’ state are summarized in Table 2. The ‘G’ state is always more stable than the nonmagnetic ‘N’ state, but electron doping progressively reduces their energy difference. Additionally, multi-phase states, (e.g., ‘G + N’ state), with energies lying between the nonmagnetic and single-phase ‘G’ state can be found near the metal-insulator phase boundary. The ‘C’ state is generally very close in energy to the ‘G’ state in the doped compounds, considering the resolution of these calculations. Because the ‘C’ state does not improve the values of $N(0)$ with respect to the ‘G’ state, we use the latter as reference for analysis of the multiphase states.

4.4.2 The ‘G+E’ multiphase state at $x = 0.0625$

In Figure 5, we highlight the low-energy ‘G+E’ state found near the metal-insulator phase boundary at $x = 0.0625$ [5]. This multiphase state is similar to the single-phase ‘G’ state, except that the magnetic moments at the corner Cu atoms are sign reversed (orange vectors). The size of magnetic moments at copper sites is also less uniformly distributed in the cell: the ‘G’ state has magnetic moments at copper site of $\pm 0.396 - 0.412\mu_B$ per atom while the ‘G+E’ state has magnetic moments at copper sites of $\pm 0.309 - 0.394\mu_B$ per atom.

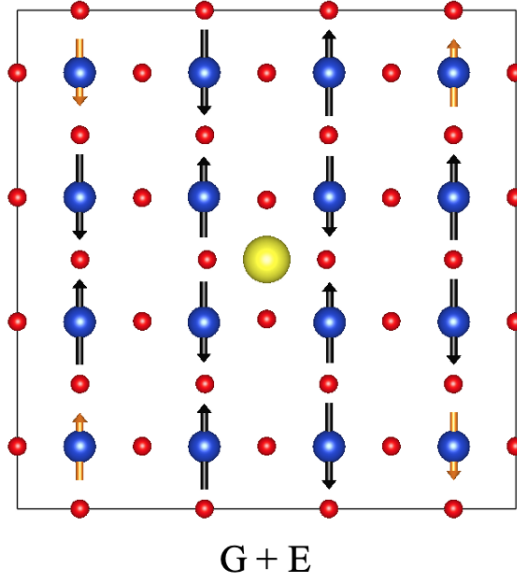


Figure 5: The top view from a $4 \times 4 \times 2$ supercell in the ‘G+E’ state for SLCO with $x = 0.0625$. The Sr atoms have been omitted for clarity. La dopants are shown as central yellow spheres. The orange-colored vectors denote the reversed magnetic moments at the corner Cu atoms. The vector size is scaled to the magnetic moment strength. In this illustration, the magnetic moments are assumed to be aligned within the CuO_2 plane.

Estimation of magnetic exchange coupling parameter J

Here, the energy difference between ‘G + E’ and ‘G’ states is used to estimate the magnetic exchange coupling parameter J . We consider the total energy of a periodic supercell containing N magnetic atoms to consist of a nonmagnetic part E_0 and magnetic part E_{mag} :

$$E(N \text{ magnetic atoms}) = E_0 + E_{\text{mag}} \quad (2)$$

The following approximation based on spin- $\frac{1}{2}$ nearest-neighbor (NN) 2D Ising model is used for E_{mag} :

$$E_{\text{mag}} = \text{no. of FM NN pairs} \times \left(\frac{J}{4}\right) + \text{no. of AFM NN pairs} \times \left(\frac{-J}{4}\right) \quad (3)$$

The energy difference of these states can be computed as:

$$\begin{aligned} \Delta E_{\text{G+E}',\text{G}'} &= \Delta E_0 + \Delta E_{\text{mag}} \\ &\approx \frac{J}{4} \times (\Delta [\text{no. of FM NN pairs}] - \Delta [\text{no. of AFM NN pairs}]) \end{aligned} \quad (4)$$

where $\Delta E_0 \ll \Delta E_{\text{mag}}$ is assumed based on their similar atomic configurations. Going from the ‘G’ state to ‘G+E’ state for the supercell of 32 magnetic Cu atoms as depicted in Figure 5 involves changing 16 pairs from AFM to FM ordering. Therefore, $\Delta(\text{no. of FM NN pairs}) = 16$ and $\Delta(\text{no. of AFM NN pairs}) = -16$, which gives:

$$\Delta E_{\text{G+E}',\text{G}'}(32 \text{ Cu atoms}) = 8J \quad (5)$$

We normalize this formula to work with the values listed in Table 2:

$$J = 4 \times (E_{\text{G+E}'}^{\text{per atom}} - E_{\text{G}'}^{\text{per atom}}) = 127.08 \text{ meV} \quad (6)$$

which is comparable with measurements of other cuprates possessing similar superconducting transition temperature (T_c) values (Table 3).

System	carrier	T_c^{max} (K)	J (meV)	Remark
Nd-CCO	electrons	24	126, 155	Expt. [34, 35]
Pr-CCO	electrons	22	106, 130, 121	Expt. [34, 35, 36]
Sm-CCO	electrons	20	110	Expt. [37]
Bi2201	holes	34	143	Expt. [38]
La214	holes	39	133 (138)	Expt. [35] (DFT [17])
IL-SLCO	electrons	42	127	DFT - This work

Table 3: The values for magnetic exchange coupling parameter J per Cu atom.

Density of states at Fermi level $N(0)$

We show the density of states from the ‘G’ and ‘G + E’ state in Figure 6.

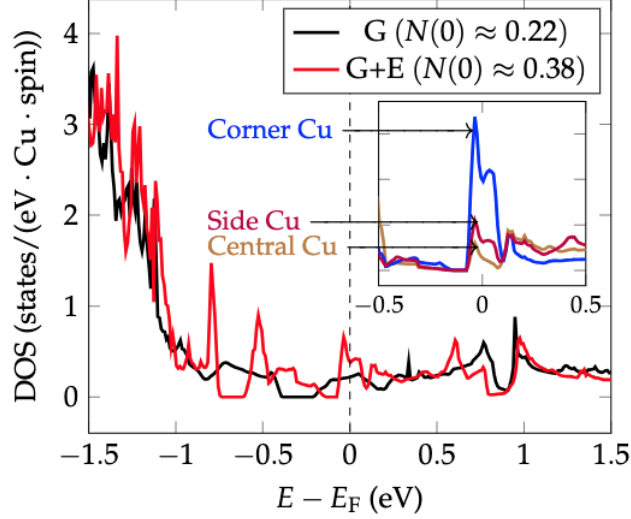


Figure 6: The DOS per Cu atom of ‘G and G + E’ configurations for SLCO with $x = 0.0625$, $4 \times 4 \times 2$ supercell. The Fermi level is set to zero. Only the spin-up DOS is shown. Inset: The spin-up DOS contributions of single Cu atom with negative moments from various Cu sites in the ‘G+E’ state.

$N(0)$ is enhanced by almost 73 percent in the ‘G+E’ state relative to the ‘G’ state. Moreover, a peak exists close to E_F with $N_{G+E}(-0.035) \approx 3N_G(0)$ which would be beneficial for superconductivity. According to atom-resolved PDOS, this increase is due to the corner Cu atoms. In particular, the total DOS for the positive spin orientation has a peak at Fermi level at Cu sites with negative spin orientations, and vice versa (see inset of Figure 6). Considering its low-energy nature, this result suggests an enhancement mechanism for $N(0)$ arising from spin fluctuations. At finite temperatures, the single-phase ground state would mix with the low-energy states and then the Cu states will be shifted towards the Fermi level with an effect of enhancing $N(0)$. This will work in favor of Cooper pair formation.

4.4.3 The ‘G+N’ state at $x = 0.125$

On the left part of Figure 7, we highlight the low-energy ‘G+N’ state at $x = 0.125$ in comparison to the ‘G’ state. The state consists of magnetic CuO_2 planes in the ‘G’ configuration for atoms closest to La dopants sandwiched by nonmagnetic planes. The magnetic moments at copper sites for the closest planes are similar in both the ‘G’ and ‘G+N’ states ($\pm 0.33\mu_B$ per Cu) and they indicate a weakened antiferromagnetic order relative to the parent compounds. As listed in Table 2, the ‘G+N’ state lies approximately 22.79 meV above the ‘G’ state. The appearance of nonmagnetic planes may reflect the spin dilution effects in which electron doping results in replacement of some Cu^{2+} by Cu^+ spinless ions, as also suggested in the AMR studies in Ref. [7]. Besides, such ‘coexistence’ of magnetic and nonmagnetic planes in layered compounds was also experimentally reported in the hole-doped, Hg-based cuprates, in which some layers retain strong AFM order while the others become superconducting [39].

The DOS for the ‘G+N’ configuration is shown on the right-hand side of Figure 7. It is apparent that the nonmagnetic and magnetic layers contribute to the total DOS distinctly. For example, a gap exists around $E - E_F \approx -0.5$ eV only on the ‘G’ layers (blue traces) and not on the ‘N’ layers (red traces). The gap displacement to a lower energy is consistent with the electron doping condition. Although not as significant as the previous case, here we also note a 40.6% increase of $N(0)$ for the ‘G+N’ state relative to the ground state.

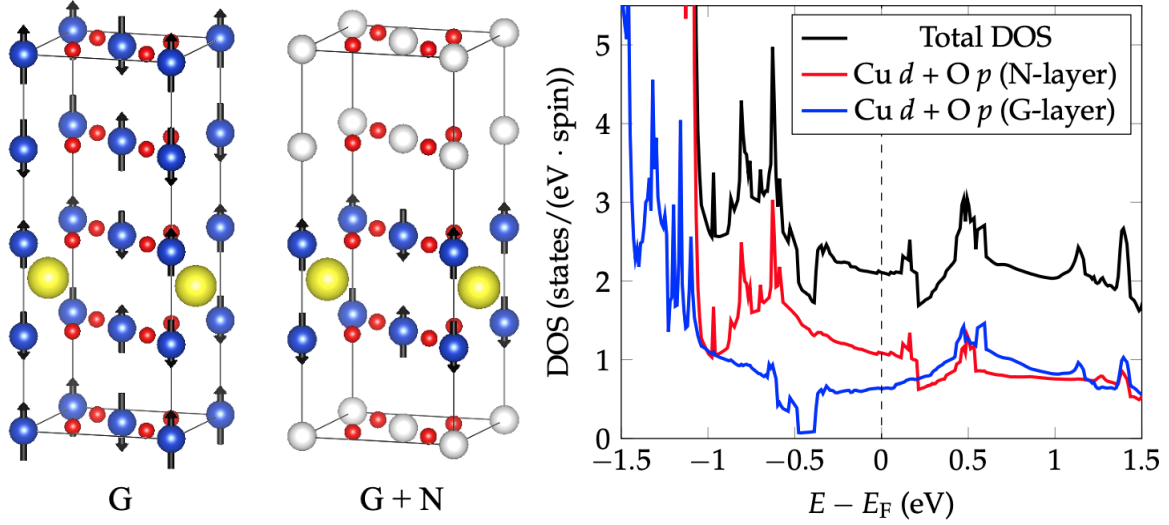


Figure 7: Left: The $\sqrt{2} \times \sqrt{2} \times 4$ supercell in the ‘G’ and ‘G+N’ states for SLCO with $x = 0.125$. The Sr atoms have been omitted for clarity. La dopants and nonmagnetic Cu atoms are each shown as yellow and white spheres. The vector size is scaled to the magnetic moment strength. The magnetic moments are assumed to be aligned normal to the CuO₂ planes in this illustration. Right: The total DOS (in black) for ‘G + N’ state. The Fermi level is set to zero. Projected DOS to the Cu d and O p orbitals from magnetic and non-magnetic planes are shown in blue and red traces, respectively.

4.4.4 The ‘G+C+N’ state at $x = 0.1$

In Figure 8, we highlight the ‘G+C+N’ state against the ‘G’ state in a $\sqrt{2} \times \sqrt{2} \times 10$ supercell. The new state consists of the nearest CuO₂ planes surrounding the La dopants in ‘C’ magnetic configuration, sandwiched by planes taking ‘G’ ordering. The magnetic moment at copper sites varies between $0.3 - 0.43\mu_B$. Interestingly, the four planes surrounding each dopant atom form domains separated by a nonmagnetic plane instead of merging in a continuous ‘G’ ordering. The AFM order thus appears inhomogeneously in a short length scale; this may be related to the loss of NMR intensity [10] mentioned in the Introduction. In the ‘G+C+N’ state, the density of states at the Fermi level, $N(0)$, is increased by 8.67 % to 0.211 states/(eV · spin · Cu atom) relative to the ‘G’ state.

Specific heat coefficient

We estimate the Sommerfeld parameter γ of electronic specific heat, defined as [40]:

$$C_{\text{el}}(T \rightarrow 0) = \gamma T \quad (7)$$

$$\gamma = \frac{2}{3} \pi^2 k_B^2 N(0) \quad (8)$$

where the DOS at Fermi level $N(0)$ is defined per atom and per one spin direction. This quantity in the normal state extrapolated to zero temperature can be estimated from $N(0)$ of a computational cell containing X formula units [40]:

$$\gamma_n^0 (\text{mJ/K}^2 \cdot \text{mol}) \approx 2.36 \times 2N(0) (\text{state/eV} \cdot X) \quad (9)$$

Ref. [41] measured the Sommerfeld parameter of SLCO ($x = 0.1$) to be $1.04 \pm 0.01 (\text{mJ/K}^2 \cdot \text{mol})$. Hence, there is a good agreement between the experimental value with our estimation of 0.918 and 0.996 $\text{mJ/K}^2 \cdot \text{mol}$ for the ‘G’ and ‘G+C+N’ states, respectively.

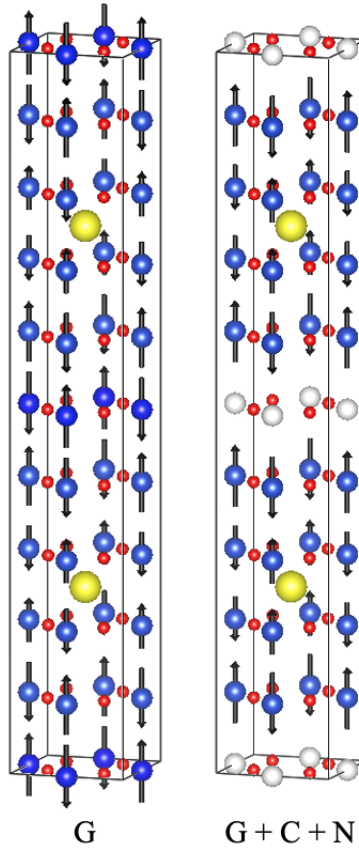


Figure 8: The $\sqrt{2} \times \sqrt{2} \times 10$ supercell in the ‘G’ and ‘G+C+N’ states for SLCO with $x = 0.1$. The Sr atoms have been omitted for clarity. La dopants and nonmagnetic Cu atoms are shown as yellow and white spheres, respectively. The vector length is scaled to the magnetic moment. The magnetic moments are assumed to be aligned normal to the CuO_2 planes in this illustration.

4.4.5 Pressure effects

Unlike hole-doped cuprates, pressure effects in the electronic structure of electron-doped compounds are reported to be much weaker [42, 43, 44]. No pressure dependence on T_c and several other parameters for $\text{Sr}_{0.9}\text{La}_{0.1}\text{CuO}_2$ are observed up to 1 GPa [45, 46]. As far as we know, there is only a report of small increase of 3K ($\approx 7\%$) for $\text{Sr}_{0.9}\text{La}_{0.1}\text{CuO}_2$ measured at high pressure of 15 GPa in Ref. [43]. All of the pressure studies involving SLCO were performed with hydrostatic pressure, where both a and c lattice parameters get compressed. Uniaxial pressure studies on this material have not been available.

Here, we perform electronic structure calculations for the ‘G’ state under hydrostatic (P_{all}), in-plane (P_{ab}), and uniaxial c -axis (P_c) compressions. The former is executed with a built-in feature of the VASP code, while the directional compressions are performed by taking the optimized ‘G’ structure at zero pressure as a base, reducing the respective lattice parameters, and reoptimizing relative coordinates for the DOS calculations. The results are illustrated in Figure 9, where we have plotted the values of $N(0)$ alongside their respective estimation for γ_n^0 following equation (9). The pressure effects to $N(0)$ are generally very weak. We note a small increase with uniaxial c -axis compression P_c , but not P_{all} or P_{ab} .

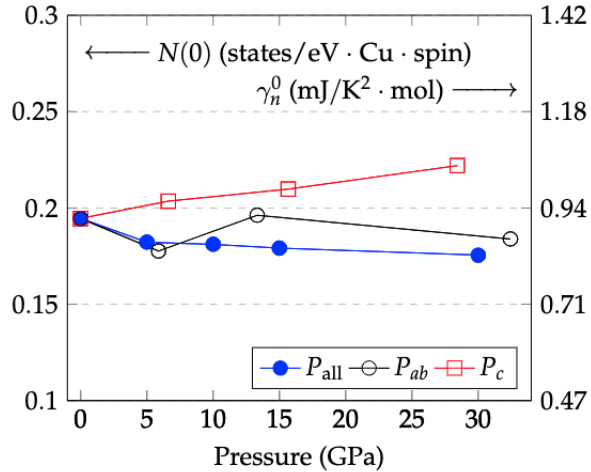


Figure 9: The density of states at Fermi level, $N(0)$ and the estimated specific heat coefficient, γ_n^0 , for $\text{Sr}_{0.9}\text{La}_{0.1}\text{CuO}_2$ in the ‘G’ state under hydrostatic (P_{all}), in-plane (P_{ab}), and uniaxial c -axis (P_c) compressions.

Parameter	0	5 GPa	10 GPa	15 GPa	30 GPa
a	3.927	3.890	3.861	3.836	3.778
c	3.425	3.357	3.298	3.244	3.120

Table 4: The lattice parameters for $\text{Sr}_{0.9}\text{La}_{0.1}\text{CuO}_2$ under hydrostatic compressions.

Under hydrostatic compressions, the values of a and c are both reduced as shown in Table 4. From these results, the effects of in-plane compression to $N(0)$ are likely to be stronger than c -axis compression when both are present. We look at these results with the evolution of a and c under doping x shown in Figure 4. Although the La concentration here is fixed at $x = 0.1$, the reduced a (c) is akin to moving towards lesser (higher) doping. It is possible that introducing La dopant atoms will have an effect similar to applying pressure, which will be an interesting issue to be studied in the future.

Although $N(0)$ appears to be increasing monotonously with P_c , it is difficult to connect this result with the pressure dependence of T_c . The changes are minute, and the correlation between $N(0)$ and T_c is more subtle in cuprates than in the conventional superconductors. On the other hand, the uniaxial pressure dependence for T_c in electron-doped cuprates itself is not yet established. For example, studies of Sm-CCO [47] deduced that decreasing c (a) has small positive (negative) effects on T_c . However,

the study for Nd-CCO suggested the opposite effect [48]. The effects of uniaxial compression may also differ in SLCO as it is not isostructural with these compounds. Hence, we encourage further experimental investigations of uniaxial stress in SLCO.

4.4.6 A nontrivial dopant role ?

In the single phase ‘G’ states, the magnetic moment at Cu sites closer to the La dopant is weaker than the others. This can be explained by a larger carrier doping in these sites, concurring with the observation in hole-doped layered cuprates [20, 39, 49]. However, this is not always true for the multiphase examples. The role of the dopant is likely to be more complex than simply distributing free charge carriers as a function of distance from its location. Further studies involving comparison between dopant species may elucidate this aspect in the future.

Finally, we remark that the multiphase states showcased in this brief work are preliminary examples which do not form an exhaustive list. Additional states could be found with more extensive calculations. It is plausible that more competitive states with highly enhanced $N(0)$ exist at suitable x values. We believe they could be interesting precursor candidates for superconductivity of magnetic origin.

5 Conclusions

In this brief work, we study the electron-doped, infinite-layer $\text{Sr}_{1-x}\text{La}_x\text{CuO}_2$ using first-principles SCAN density functional calculations. The optimized crystal structures concur with experimental trends against x , achieving a better agreement in lattice parameters than its functional predecessors. The parent compound is confirmed to be an antiferromagnetic insulator which becomes metallic upon La substitution. Low-energy configurations of multiphase states with interesting magnetic and electronic structure are found in the doped compounds. These states can mix with the single-phase ground state at finite temperatures, leading to enhanced density of states at Fermi level due to spin fluctuations. The validity of our calculations are also supported by good agreement with commonly measured quantities, such as the magnetic exchange coupling parameter and the specific heat coefficient. By means of a simple pressure study, we find a small positive effect of uniaxial c -axis compressions on the electronic structure characterized by $N(0)$. We believe that further studies of exotic magnetic states may help explain the mechanism for various correlated phenomena of these materials in the future.

Acknowledgments

The calculations were performed with the facilities of the Supercomputer Center, the Institute for Solid State Physics, the University of Tokyo.

Declaration of competing interest

The authors have no conflicts to disclose.

References

- [1] J. G. Bednorz, K. A. Müller, *Z. Phys. B: Condens. Matter* 64 (1986) 189.
- [2] W. E. Pickett, *Rev. Mod. Phys.* 61 (1989) 433–512.
- [3] A. Damascelli, Z. Hussain, Z.-X. Shen, *Rev. Mod. Phys.* 75 (2003) 473–541.
- [4] N. P. Armitage, P. Fournier, R. L. Greene, *Rev. Mod. Phys.* 82 (2010) 2421–2487.
- [5] P. Fournier, *Physica C* 514 (2015) 314–338.
- [6] M. Naito, Y. Krockenberger, A. Ikeda, H. Yamamoto, *Physica C* 523 (2016) 28–54.
- [7] V. P. Jovanović, L. Fruchter, Z. Z. Li, H. Raffy, *Phys. Rev. B* 81 (2010) 134520.
- [8] J. D. Jorgensen, P. G. Radaelli, D. G. Hinks, J. L. Wagner, S. Kikkawa, G. Er, F. Kanamaru, *Phys. Rev. B* 47 (1993) 14654–14656.
- [9] V. P. Jovanović, H. Raffy, Z. Z. Li, G. Reményi, P. Monceau, *Phys. Rev. B* 103 (2021) 014520.
- [10] G. V. M. Williams, J. Haase, M.-S. Park, K. H. Kim, S.-I. Lee, *Phys. Rev. B* 72 (2005) 212511.
- [11] K. H. Satoh, S. Takeshita, A. Koda, R. Kadono, K. Ishida, S. Pyon, T. Sasagawa, H. Takagi, *Phys. Rev. B* 77 (2008) 224503.
- [12] J. W. Harter, L. Maritato, D. E. Shai, E. J. Monkman, Y. Nie, D. G. Schlom, K. M. Shen, *Phys. Rev. Lett.* 109 (2012) 267001.
- [13] W. Yu, J. S. Higgins, P. Bach, R. L. Greene, *Phys. Rev. B* 76 (2007) 020503.
- [14] C. Ambrosch-Draxl, K. Schwarz, *Solid State Commun.* 77 (1991) 45–48.
- [15] J. Sun, A. Ruzsinszky, J. P. Perdew, *Phys. Rev. Lett.* 115 (2015) 036402.
- [16] J. W. Furness, Y. Zhang, C. Lane, I. G. Buda, B. Barbiellini, R. S. Markiewicz, A. Bansil, J. Sun, *Commun. Phys.* 1 (2018) 1–6.
- [17] C. Lane, J. W. Furness, I. G. Buda, Y. Zhang, R. S. Markiewicz, B. Barbiellini, J. Sun, A. Bansil, *Phys. Rev. B* 98 (2018) 125140.
- [18] Y. Zhang, C. Lane, J. W. Furness, B. Barbiellini, J. P. Perdew, R. S. Markiewicz, A. Bansil, J. Sun, *Proc. of the Nat'l Acad. of Sci.* 117 (2020) 68–72.
- [19] J. Nokelainen, C. Lane, R. S. Markiewicz, B. Barbiellini, A. Pulkkinen, B. Singh, J. Sun, K. Pussi, A. Bansil, *Phys. Rev. B* 101 (2020) 214523.
- [20] A. N. Tatan, J. Haruyama, O. Sugino, *AIP Advances* 12 (2022) 105308.
- [21] G. Kresse, D. Joubert, *Phys. Rev. B* 59 (1999) 1758–1775.
- [22] G. Kresse, J. Hafner, *Phys. Rev. B* 48 (1993) 13115–13118.
- [23] G. Kresse, J. Furthmüller, *Phys. Rev. B* 54 (1996) 11169–11186.
- [24] P. E. Blöchl, O. Jepsen, O. K. Andersen, *Phys. Rev. B* 49 (1994) 16223–16233.
- [25] E. O. Wollan, W. C. Koehler, *Phys. Rev.* 100 (1955) 545–563.
- [26] R. Zhang, C. Lane, B. Singh, J. Nokelainen, B. Barbiellini, R. S. Markiewicz, A. Bansil, J. Sun, *Commun. Phys.* 4 (2021) 118.
- [27] E. Dagotto, J. Burgu, A. Moreo, *Solid State Commun.* 126 (2003) 9–22.
- [28] E. Dagotto, *Nanoscale phase separation and colossal magnetoresistance: the physics of manganites and related compounds*, Springer Science & Business Media, 2003.

- [29] A. O. Sboychakov, S. Savel'ev, A. L. Rakhmanov, K. I. Kugel, F. Nori, *Phys. Rev. B* 77 (2008) 224504.
- [30] G. E. S. Kikkawa, F. Kanamaru, Y. Miyamoto, S. Tanaka, M. Sera, M. Sato, Z. Hiroi, M. Takano, Y. Bando, *Physica C* 196 (1992) 271–275.
- [31] A. M. Ganose, A. J. Jackson, D. O. Scanlon, *Journ. of Open Source Software* 3 (2018) 717.
- [32] M. Boehm, S. Coad, B. Roessli, A. Zheludev, M. Zolliker, P. Böni, D. M. Paul, H. Eisaki, N. Motoyama, S. Uchida, *Europhysics Letters* 43 (1998) 77.
- [33] D. Mertz, R. Hayn, I. Opahle, H. Rosner, *Phys. Rev. B* 72 (2005) 085133.
- [34] M. Matsuda, K. Yamada, K. Kakurai, H. Kadowaki, T. R. Thurston, Y. Endoh, Y. Hidaka, R. J. Birgeneau, M. A. Kastner, P. M. Gehring, A. H. Moudden, G. Shirane, *Phys. Rev. B* 42 (1990) 10098–10107.
- [35] P. Bourges, H. Casalta, A. S. Ivanov, D. Petitgrand, *Phys. Rev. Lett.* 79 (1997) 4906–4909.
- [36] I. W. Sumarlin, J. W. Lynn, T. Chattopadhyay, S. N. Barilo, D. I. Zhigunov, J. L. Peng, *Phys. Rev. B* 51 (1995) 5824–5839.
- [37] P. E. Sulewski, P. A. Fleury, K. B. Lyons, S.-W. Cheong, Z. Fisk, *Phys. Rev. B* 41 (1990) 225–230.
- [38] Y. Peng, G. Dellea, M. Minola, M. Conni, A. Amorese, D. Di Castro, G. De Luca, K. Kummer, M. Salluzzo, X. Sun, et al., *Nature Physics* 13 (2017) 1201–1206.
- [39] H. Kotegawa, Y. Tokunaga, Y. Araki, G.-q. Zheng, Y. Kitaoka, K. Tokiwa, K. Ito, T. Watanabe, A. Iyo, Y. Tanaka, H. Ihara, *Phys. Rev. B* 69 (2004) 014501.
- [40] N. Plakida, *High-Temperature Cuprate Superconductors*, Springer Berlin Heidelberg, 2010. doi:[10.1007/978-3-642-12633-8](https://doi.org/10.1007/978-3-642-12633-8).
- [41] Z. Y. Liu, H. H. Wen, L. Shan, H. P. Yang, X. F. Lu, H. Gao, M.-S. Park, C. U. Jung, S.-I. Lee, *Europhysics Letters* 69 (2004) 263.
- [42] C. Murayama, N. Mori, S. Yomo, H. Takagi, S. Uchida, Y. Tokura, *Nature* 339 (1989) 293–294.
- [43] S. Ishiwata, D. Kotajima, N. Takeshita, C. Terakura, S. Seki, Y. Tokura, *Journal of the Physical Society of Japan* 82 (2013) 063705.
- [44] H. Takahashi, N. Mōri, M. Azuma, Z. Hiroi, M. Takano, *Physica C: Superconductivity* 227 (1994) 395–398.
- [45] D. D. Castro, R. Khasanov, A. Shengelaya, K. Conder, D.-J. Jang, M.-S. Park, S.-I. Lee, H. Keller, *Journal of Physics: Condensed Matter* 21 (2009) 275701.
- [46] H. Kim, M.-H. Kim, M. Jung, M.-S. Park, S.-I. Lee, *Physica B: Condensed Matter* 378-380 (2006) 886–887. Proceedings of the International Conference on Strongly Correlated Electron Systems.
- [47] M. Kund, J. Neumeier, K. Andres, J. Markl, G. Saemann-Ischenko, *Physica C: Superconductivity* 296 (1998) 173–178.
- [48] Y. Kaga, T. Sasagawa, S. Takahashi, K. Unosawa, H. Takagi, *Physica B: Condensed Matter* 359-361 (2005) 442–444. Proceedings of the International Conference on Strongly Correlated Electron Systems.
- [49] H. Mukuda, M. Abe, Y. Araki, Y. Kitaoka, K. Tokiwa, T. Watanabe, A. Iyo, H. Kito, Y. Tanaka, *Phys. Rev. Lett.* 96 (2006) 087001.